Use of Sentinel-1 C-Band SAR Images for Convective System Surface Wind Pattern Detection

TRAN VU LA, CHRISTOPHE MESSAGER, MARC HONNORAT, AND RÉMI SAHL

Extreme Weather Expertises, Brest, France

ALI KHENCHAF

Lab-STICC, UMR CNRS 6285, ENSTA Bretagne, Brest, France

CLAIRE CHANNELLIERE AND PHILIPPE LATTES

TOTAL Exploration and Production, La Défense, Courbevoie, France

ABSTRACT

Convective systems (CS) through their downdrafts hitting the sea surface may produce wind patterns (or cold pools) with wind intensity exceeding 10–25 m s^{-1}. The latter for a long time have been significant for weather forecast and meteorological studies, especially in the tropical regions like the Gulf of Guinea since it is hard to detect the CS-associated wind patterns. Based on Sentinel-1 images [C-band Synthetic Aperture Radar (SAR)] with high spatial resolution and large swath, the current study proposed the detection of surface wind patterns through wind speed estimation by C-band model 5.N (CMOD5.N; for vertically polarized images) and two models proposed by Sapp and Komarov (for horizontally polarized images). Relative to the X-band SAR, the effects of precipitation on C-band radar backscattering are negligible, and thereby it has little impact on wind speed estimation from Sentinel-1 images. The detected surface wind patterns include a squall line and a bow echo at the mesoscale (>100 km) and many submesoscale (<100 km) convection cells. They are accompanied by various degrees of precipitation (from light to heavy rain). This study also used Meteosat infrared images for monitoring and detection of deep convective clouds (with low brightness temperature) corresponding to surface wind patterns. The agreement in location and sometimes in shape between them strengthened the assumption that the CS downdrafts may induce the sea surface patterns with high wind intensity (10–25 m s^{-1}). In particular, because of the Sentinel-1 high spatial resolution, the pattern spots with high winds (20–25 m s^{-1}) are detected on the illustrated images, which was not reported in the literature. They are located close to the coldest convective clouds (about 200-K brightness temperature).

1. Introduction

Convective systems (CS) produce meteorological hazards over the land and sea surfaces such as strong surface winds, lightning, and heavy rainfall (Mohr et al. 2017; Kastman et al. 2017). While some radar devices can measure intense precipitation caused by the CS, the associated strong surface winds (or gusts) are difficult to estimate since they happen suddenly (Portabella et al. 2012). In fact, in the mature or decaying phase of CS, the air that is cooled by precipitation falls and hits the surface (thus called downdraft), where it can induce strong surface winds in a short time, and normally in the form of cold pools (or wind patterns). The intensity and evolution time of wind gusts depends on the CS severity and synoptic winds.

Some references (King et al. 2017; Priftis et al. 2018) proposed the use of C-band scatterometers (ASCAT-A/B) for the estimation of wind fields associated with the CS. These studies illustrated that within the convective core surface wind speed exceeds 20 m s^{-1}, as also indicated in Mohr et al. (2017), Cotton et al. (2011), and Kuchera and Parker (2006). However, according to Kilpatrick and Xie (2015), ASCAT can only detect wind patterns produced by the mesoscale downdrafts (100–300 km) whereas they cannot identify the convective-scale gust fronts (5–20 km) because of their large spatial resolution (12.5–25-km wind grid). In general, the wind speed associated with

the mesoscale downdrafts is lower than that produced by the convective-scale ones. Synthetic Aperture Radar (SAR) devices were not recently mentioned with regard to the detection of surface winds associated with the CS. Alpers et al. (2016) discussed the observation of the convective rain cells on many SAR images, but this reference did not show the detailed results of surface wind patterns induced by the CS downdrafts. Based on the advantages of SAR, including high spatial resolution, wide swath, and availability in most weather conditions, the current paper proposes the detection of the CS-associated surface wind patterns and the estimation of wind intensity from C-band Sentinel-1 SAR images. Indeed, thanks to large swath (100–400 km), Sentinel-1 can detect surface wind patterns at multiple scales, including mesoscale ($\geq$100 km), submesoscale (<100 km), and convection cells (several kilometers). Likewise, the high spatial resolution of Sentinel-1 SAR enables the observation of wind pattern shapes, in particular the detection of small-scale parts (convective scale) of surface wind patterns that were not observed by the ASCAT. Additionally, Sentinel-1 can acquire data in most weather conditions, which is significant for the cases when both strong winds and intense precipitation occur under the CS. The effects of rainfall are negligible for C-band SAR, as indicated in Contreras and Plant (2006) and Xu et al. (2015).

Surface wind fields significantly affect sea surface roughness that can be observed by the SAR images and quantified by radar backscattering represented by normalized radar cross section (NRCS). Based on this relation, the empirical models, such as Doppler centroid (Mouche et al. 2012), azimuth wavelength cutoff (Montuori et al. 2013), and scatterometry-based functions, including a series of C-band model (CMOD; Stoffelen and Anderson 1997; Quilfen et al. 1998; Hersbach et al. 2007; Hersbach 2008), can estimate surface wind speed from SAR images. Among them, the current paper selects C-band model 5.N (CMOD5.N; Hersbach 2008) for surface wind speed retrieval since it can offer wind intensity estimates up to 25 m s^{-1} (Mouche et al. 2017), which is regularly present in the CS-associated wind patterns. The CMOD5.N function describes the relationship between the NRCS and the parameters of incidence angle, relative wind direction to radar look, and wind speed. Therefore, once the NRCS and related parameters are determined, wind speed can be estimated. Since CMOD5.N can only estimate wind speed from vertically polarized (VV-pol) SAR data, a polarization ratio (PR) is used for transforming horizontally polarized (HH-pol) data to VV-pol ones. As shown in La et al. (2017), there are some models to calculate PR, depending on the applied data. Alternatively, two models

(Sapp et al. 2016; Komarov et al. 2014) can retrieve wind speed directly from HH-pol SAR images. The Sapp model is based on CMOD5.N, while the Komarov model can estimate wind speed without wind direction input. This study selects two HH-pol models for wind speed estimation to avoid using PR.

Some factors can affect the accuracy of the SAR-based wind speed retrieval, such as wind direction uncertainty, SAR image quality (speckle noise, thermal noise, etc.), and precipitation. As shown in La et al. (2017), a 15°–30° deviation of wind direction may induce a 2 m s^{-1} difference in wind speed estimation depending on wind intensity. In the current paper, the Global Forecast System (GFS) data with a 25-km spatial grid is used to extract wind direction used in CMOD5.N. La et al. (2018) showed that the GFS wind directions were very close to the in situ data measured by the National Oceanic and Atmospheric Administration (NOAA) buoys in the Gulf of Mexico. Likewise, the estimated wind speeds by the Sapp model (with the GFS wind direction input) and the Komarov one (without wind direction input) were very close, and they also agreed with the in situ measurements. This illustrates that the GFS-based wind direction should not be a major error source for wind speed estimation. In addition to GFS, wind direction may be extracted directly from SAR images through the methods of local gradient (Koch 2004), Fourier fast transform (Fetterer et al. 1998), and continuous wavelet transform (Du et al. 2002). Although those methods can offer wind directions with a higher spatial resolution, they are not relevant for operational processing since the accuracy of the extractions depends on many factors, including image resampling ratio, speckle noise level, and data type with various spatial resolutions (La et al. 2017). Precipitation, often coupled with the CS downdrafts, may also induce a bias in wind speed estimation since it may modify radar backscattering (enhance or decrease). Rainfall effects on radar backscattering depend on rain rate, relationship to local wind speed, and particularly on radar frequency. Radar backscattering is little affected by precipitation in L band even under intense rainfall (Alpers et al. 2016), but it becomes significant for X-band radar signal (or higher frequencies). In C band, rainfall effects depend principally on local surface wind intensity, as shown in Contreras and Plant (2006) and Xu et al. (2015). It has a strong impact in cases of low winds ($\leq$7 m s^{-1}) but negligible for higher ones (>7 m s^{-1}). This is a significant conclusion for the SAR-based wind speed estimation when both strong surface winds and intense precipitation occur (regularly) under the CS impact. It illustrates that C-band SAR radar backscattering should be mainly induced from surface winds

TABLE 1. Description of Sentinel-1 Level-1 images with high resolution (HR) and medium resolution (MR) regarding four acquisition modes of stripmap (SM), interferometric swath (IWS), extrawide swath (EWS), and wave mode (WM).

Acquisition mode	Swath width (km)	Pixel size (m × m)		Spatial resolution (m × m)	
		HR	MR	HR	MR
SM	80	10 × 10	40 × 40	21–24 × 21–24	78–88 × 77–87
IWS	250	10 × 10	40 × 40	20 × 21–24	88–89 × 86
EWS	400	25 × 25	40 × 40	49–51 × 49	90–95 × 87
WM	20		25 × 25		50–52 × 50

associated with the CS downdrafts (regularly above $10 \, \mathrm{m \, s^{-1}}$) rather than by the coupled precipitation (if existing).

In addition to CS, the other events on the sea surface, such as synoptic frontogenesis (Li et al. 2015), warm-cold front (Alpers et al. 2015), and sea fetch (Li et al. 2017), may produce wind patterns close to those induced by the CS downdrafts. This can make interpreting wind patterns more difficult if only based on SAR images. Therefore, in addition to Sentinel-1, the current paper uses Meteosat Second Generation (Meteosat) infrared images for the detection of deep convective clouds that are (potentially) associated with wind patterns detected on Sentinel-1 images. Because of the differences in spatial resolution and observation time, a small deviation of spatial location between wind patterns and deep convective clouds is tolerable. With a 15-min sampling time, Meteosat may observe the evolution of most CS. This sampling time also reduces the observation time gap between Sentinel-1 and Meteosat (not over 15 min).

Section 2 presents the method of surface wind pattern detection. Section 3 illustrates many cases of the CS-associated wind patterns detected on Sentinel-1 images: (i) wind patterns accompanied by diverse precipitation intensities (light, moderate, and intense precipitation), (ii) wind patterns at multiple scales (mesoscale, submesoscale, and convection cells), and (iii) wind patterns in various shapes (squall line, bow echo, and small cells). Section 4 discusses the two parts of the detected wind patterns, the matching between the latter and deep convective clouds in terms of spatial location and observation time, and the relationship between wind patterns and precipitation. Section 5 deals with the conclusions and perspectives of this paper.

2. Method

a. Data preparation

The Sentinel-1 images used in this research are Level-1 Ground Range Detected (GRD) products (multilook),

including VV-pol and HH-pol data. Table 1 (Sentinel-1 product definition; Collecte Localisation Satellites 2016) presents the GRD images with various acquisition modes and spatial resolutions. Figure 1 presents the region of interest (the Gulf of Guinea) and Sentinel-1 images acquired over this region. They are high-resolution (HR) interferometric wide swath (IWS) products with 10-m pixel spacing and 250-km swath. Because of the large swath, these images enable the observation of wind patterns at multiple scales while high spatial resolution permits to detect the inner convective cells at a small scale (convective scale). According to the West African monsoon (WAM) seasonal cycle, the intertropical convergence zone (ITCZ) is located over the Gulf of Guinea between September and early June and then moves abruptly northward in late June (Sultan and Janicot 2003; Raj et al. 2019). Consequently, during the tropical wet period (November–June), the CS occur mainly over the West Africa coast and the Gulf of Guinea. Based on this observation, the current study uses Sentinel-1 images acquired from November 2016 to June 2017 for surface wind pattern detection.

In addition to Sentinel-1, Meteosat (2.8-km spatial resolution) is used for the detection of deep convective clouds corresponding to surface wind patterns. According to Klein et al. (2018) and Liu et al. (2007), the deepest convective clouds (or coldest ones) have the lowest brightness temperatures (200–205 K). Two Meteosat images (with the 15-min observation time difference) are used to follow the CS evolution.

To investigate the relationship between the CS downdrafts and precipitation, the Global Precipitation Measurement (GPM) data are used for rainfall estimation. They are Integrated Multisatellite Retrievals for GPM (IMERG) products with 0.1° latitude spatial resolution and 30-min temporal resolution. The difference in observation time between Sentinel-1 and GPM in this study is not over 15 min.

b. Surface wind speed estimation

Surface wind speed estimation on Sentinel-1 images is based on CMOD5.N (Hersbach 2008) for VV-pol images and two models proposed by (Komarov et al. 2014;
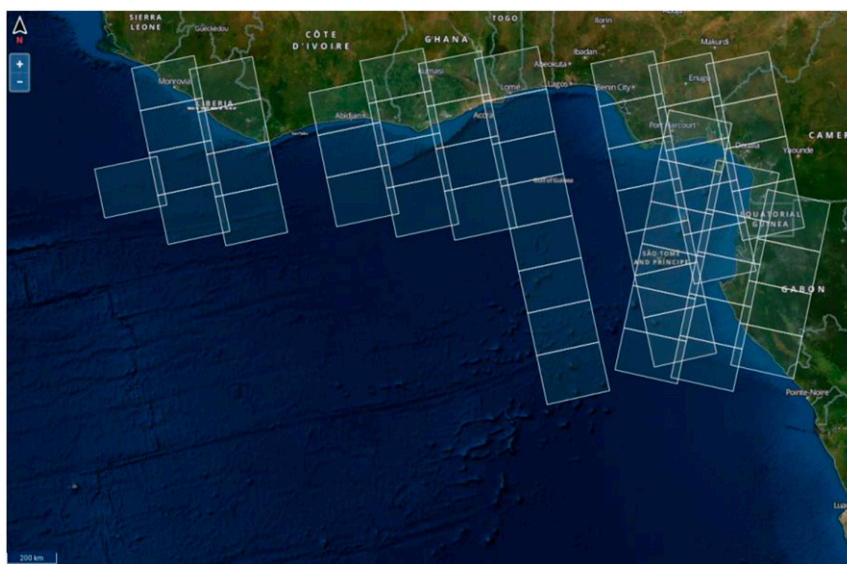
FIG. 1. Region of interest (the Gulf of Guinea) with Sentinel-1 images (GRD; IWS) acquired from 1 to 10 Mar 2017.

Sapp et al. 2016) for HH-pol images. Contrary to CMOD5.N and the Sapp model (both scatterometry-based functions), the Komarov model may estimate surface wind speed without wind direction input.

The GFS wind direction (25-km spatial grid) is used for wind speed estimation in the CMOD5.N and Sapp model in this study. Section 3 illustrates the comparison of wind speed estimates performed by the Sapp model (with the GFS wind direction input) and Komarov one (without wind direction input). This permits the evaluation of (possible) bias in wind speed estimation produced by the large-scale GFS wind directions. Precipitation may also induce important bias in wind speed estimation for winds below $7\,\mathrm{m\,s^{-1}}$ but not for higher ones above $7\,\mathrm{m\,s^{-1}}$ (Contreras and Plant 2006; Xu et al. 2015). Under the CS effects on the sea surface, including downdrafts and precipitation, radar back-scattering (or NRCS) may consist of three parts due to synoptic winds, surface gust associated with CS down-draft, and precipitation effects including atmospheric impact and impinging raindrops on the sea surface. To facilitate and simplify data processing, the NRCS due to precipitation is negligible for wind speed estimation, since its effects on radar backscattering are negligible, compared to those of strong surface winds induced by the CS downdrafts. Additionally, the NRCS extracted from Sentinel-1 images is assumed to be produced by the combination of the synoptic winds and surface gusts associated with the CS. Indeed, it is not possible (or almost) to discriminate one from the other since the interaction between regional and/or synoptic winds and

local cold pool effects at the sea surface is a complex process.

3. CS wind pattern detection and wind intensity estimation on Sentinel-1 images

This section illustrates the detection of sea surface wind patterns produced by the CS downdrafts on Sentinel-1 images from November 2016 to June 2017. This time is the monsoon period in the Gulf of Guinea (zone of interest) during which CS are the most powerful in this region (Sultan and Janicot 2003; Raj et al. 2019). Various cases of the detected wind patterns in terms of size, shape, and relationship with precipitation are illustrated in this section. Wind pattern scale can be divided into mesoscale ($\geq 100\,\mathrm{km}$), submesoscale ($<100\,\mathrm{km}$), and small cells (several kilometers). This classification does not correspond to that performed on the infrared images for the detection of deep convective clouds. Wind pattern shape can be observed as a squall line, a bow echo, and convection cells (Cotton et al. 2011; Weisman and Trapp 2003).

The precipitation coupled with the CS downdraft in the current study is classified according to Met Office (2007), including light rain ($<2\,\mathrm{mm\,h^{-1}}$), moderate rain ($2–10\,\mathrm{mm\,h^{-1}}$), heavy rain ($10–50\,\mathrm{mm\,h^{-1}}$), and violent rain ($<50\,\mathrm{mm\,h^{-1}}$). As shown in Contreras and Plant (2006) and Xu et al. (2015), the C-band radar backscattering with surface winds higher than $7\,\mathrm{m\,s^{-1}}$ is less sensitive to rain rate lower than $50\,\mathrm{mm\,h^{-1}}$.
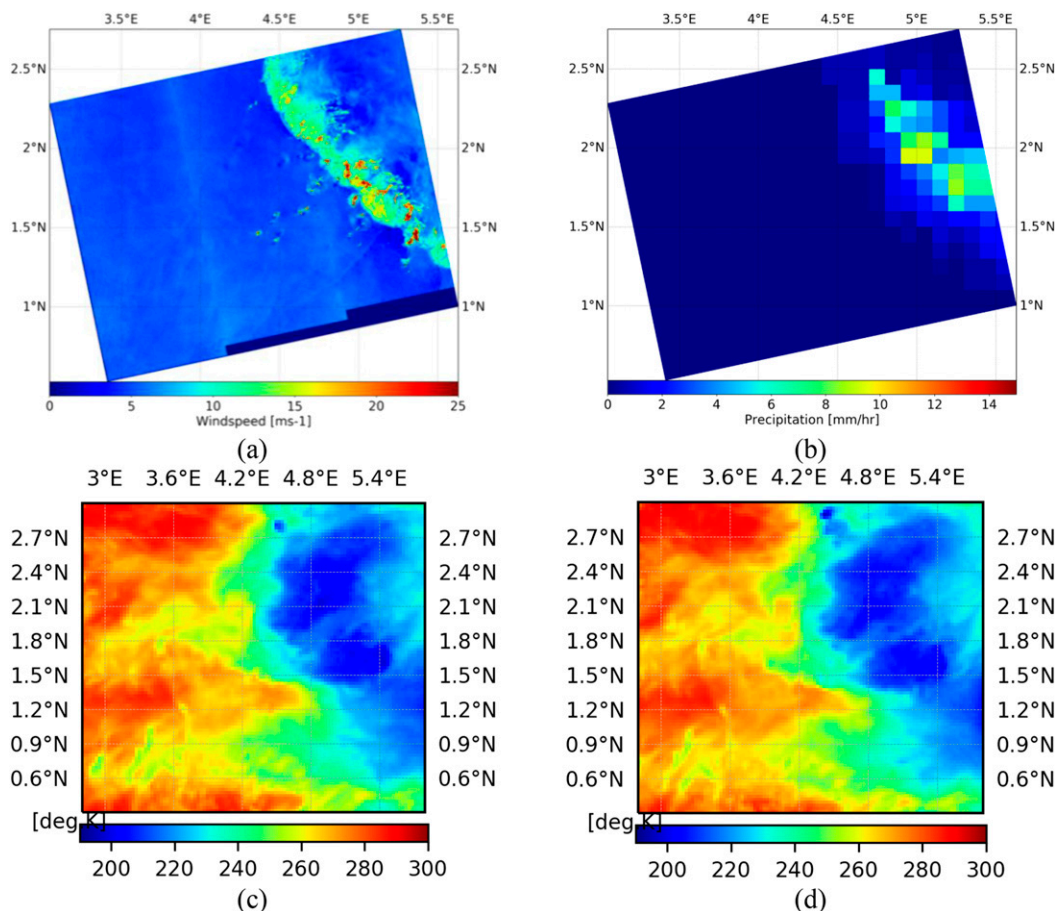
FIG. 2. Detection of mesoscale wind patterns observed as a squall line on a (VV-pol) Sentinel-1 image (IWS; GRD-HR) from 1800:06 UTC 11 Mar 2017: (a) mesoscale patterns with wind intensity (estimated by CMOD5.N) exceeding 10–20 m s^{-1}, (b) GPM–IMERG moderate precipitation (1800:00–1830:00 UTC 11 Mar 2017) coupled with the patterns in (a), and the deep convective clouds (200–220 K) on *Meteosat-11* images from (c) 1745:00 and (d) 1800:00 UTC 11 Mar 2017 corresponding to the squall line in (a).

Based on the analysis of hundreds of Sentinel-1 images (VV-pol and HH-pol) from November 2016 to June 2017, this section illustrates five representative cases of the detected CS wind patterns:

1) mesoscale wind patterns observed as a squall line accompanied by moderate precipitation on a (VV-pol) Sentinel-1 image from 1800:06 UTC 11 March 2017,
2) mesoscale wind patterns observed as a bow echo accompanied by intense precipitation on a (VV-pol) Sentinel-1 image from 1841:36 UTC 12 March 2017,
3) submesoscale wind patterns observed as small squall lines and convection cells accompanied by various precipitation on (VV-pol) Sentinel-1 images from 1800:35–1801:00 UTC 11 March 2017, and
4) submesoscale wind patterns observed as small bow echoes and convection cells accompanied by various

precipitation intensities on an (HH-pol) Sentinel-1 image from 0530:43 UTC 12 December 2016.

a. Mesoscale wind patterns observed as a squall line

Figure 2a presents mesoscale wind patterns observed on a (VV-pol) Sentinel-1 image (IWS; GRD-HR) from 1800:06 UTC 11 March 2017. It is accompanied by moderate precipitation (about 9.5 mm h^{-1}) in Fig. 2b.

Three features of wind patterns permit assumption of a squall line (Cotton et al. 2011): (i) a line consisting of vigorous convection cells, (ii) the size more than 100 km or 1° latitude (1°–2.5°N latitude, 4.5°–5.5°E longitude), and (iii) the associated wind intensity with the patterns (estimated by CMOD5.N) exceeding 15 m s^{-1}. In particular, they include some wind spots with 20–25 m s^{-1}.

The assumption of the squall line is strengthened by the detection of the corresponding deep convective
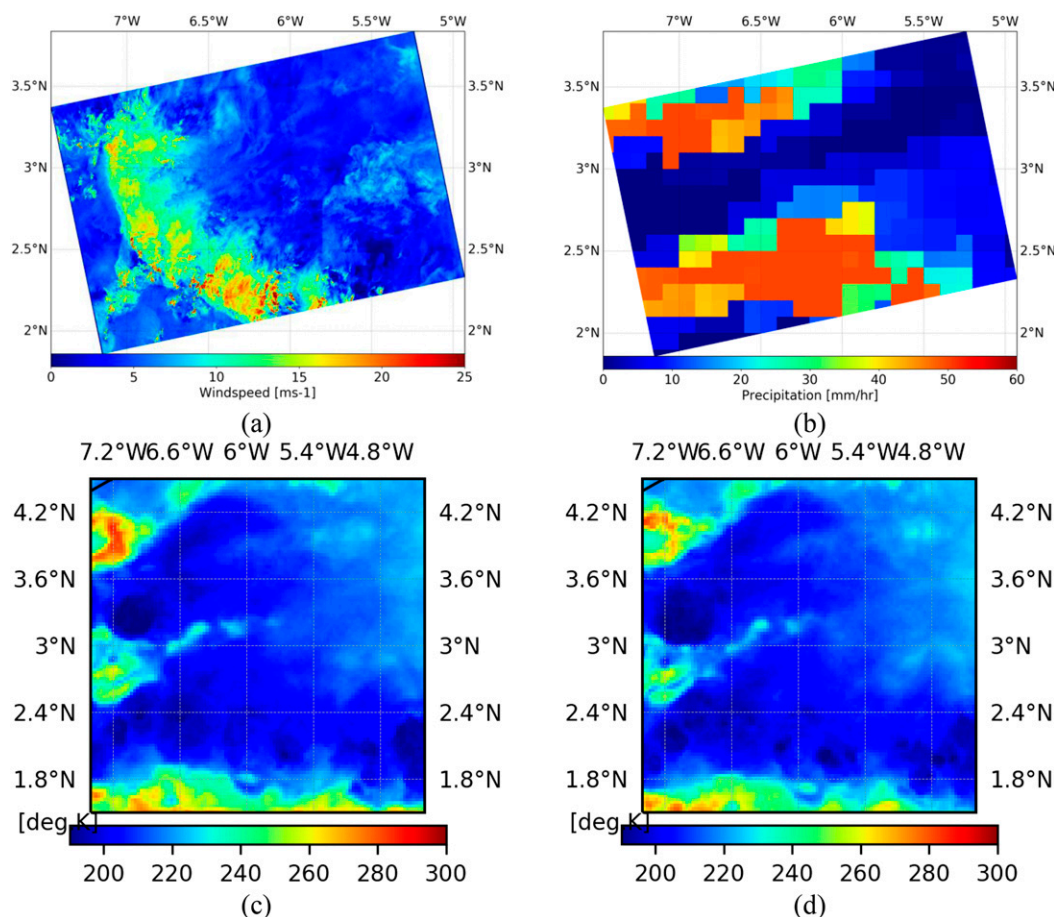
FIG. 3. (a) Detection of mesoscale wind patterns observed as a bow echo on a (VV-pol) Sentinel-1 image (IWS; GRD-HR) from 1841:36 UTC 12 Mar 2017, (b) GPM–IMERG intense precipitation of 20–50 mm h^{-1} (1830:00–1900:00 UTC 12 Mar 2017) coupled with the patterns in (a), and the deep convective clouds (200–220 K) on *Meteosat-11* images from (c) 1830:00 and (d) 1845:00 UTC 12 Mar 2017 corresponding to the bow echo in (a).

clouds (200–220 K) in Figs. 2c and 2d (1745:00 and 1800:00 UTC, respectively). During 15 min, the spatial location and shape of convective clouds are almost the same. Spatial location and observation time of surface wind patterns (Fig. 2a) and deep convective clouds are very close. Likewise, they have very similar shapes. In particular, the spots with high wind intensity (20–25 m s^{-1}) in Fig. 2a and the coldest convective ones (about 200 K) have matching spatial locations 1.8°–2°N, 4.8°–5°E and 1.5°–1.8°N, 5.4°E.

b. Mesoscale wind patterns observed as a bow echo

Figure 3a illustrates the detection of mesoscale wind patterns on a (VV-pol) Sentinel-1 image (IWS; GRD-HR) from 1841:36 UTC 12 March 2017. Their size, over 100 km or 1° latitude (2°–3.5°N latitude, 5.5°–7°E longitude), is very similar to that in Fig. 2a. Wind intensity also exceeds 15–25 m s^{-1}. However, the shape differs from that in Fig. 2a. It is called a bow echo rather than a

squall line. A bow echo is a specific subset of squall lines. It is a convection line that becomes bowed at some cycle stages into a convective arc. Three features of wind patterns (Fig. 3a) assumed as a bow echo (i.e., size, wind intensity, and especially shape) are very close to those described in Weisman and Trapp (2003). The patterns are accompanied by intense precipitation from 20 to 50 mm h^{-1} (Fig. 3b).

Figures 3c and 3d present the corresponding deep convective clouds to the wind patterns in Fig. 3a. Between 1830:00 and 1845:00 UTC, the evolution of the convective clouds is mainly noted for the spots having the lowest brightness temperature (about 200 K). In particular, the coldest convective spots have an agreement in spatial locations with those having high wind intensity (20–25 m s^{-1}), for example, in the zones about 3°N, 7°W and 2°–2.5°N, 7°–6°W. The matching in terms of spatial location between the spots with the lowest temperature and high wind intensity in this case and the
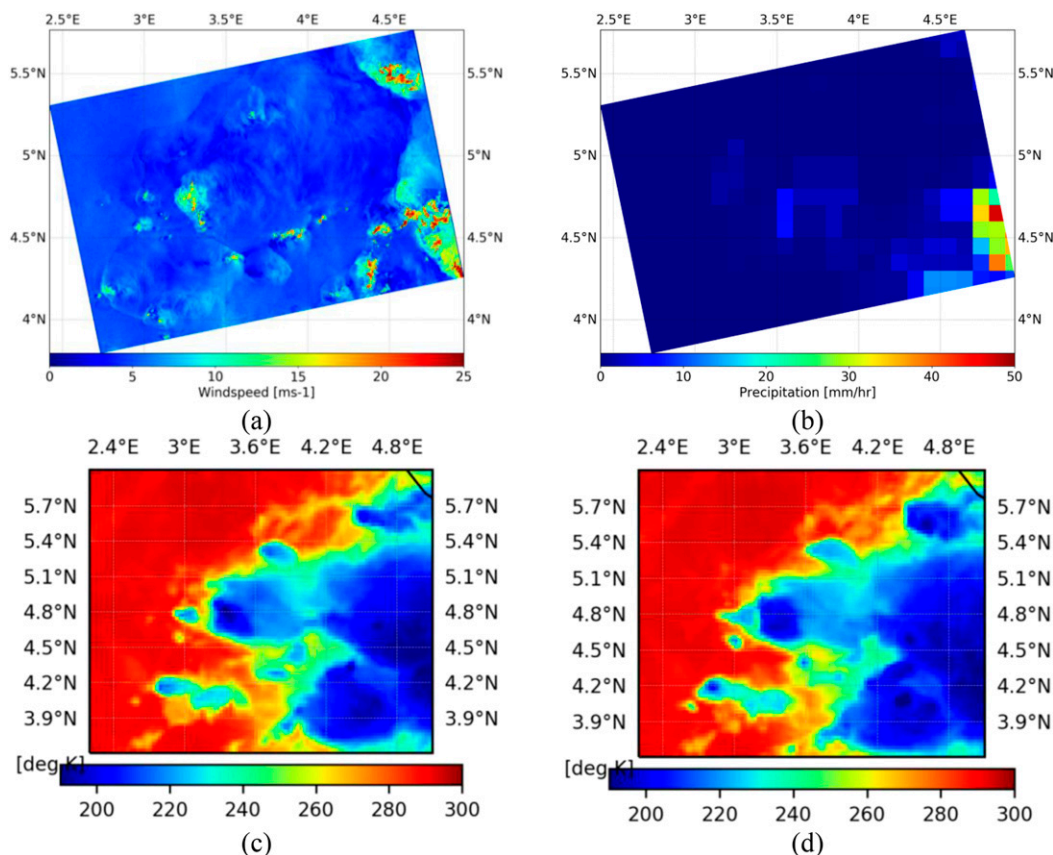
FIG. 4. (a) Detection of submesoscale wind patterns observed as a small squall line and convection cells on a (VV-pol) Sentinel-1 image (IWS; GRD-HR) from 1800:35 UTC 11 Mar 2017, (b) various GPM–IMERG precipitation of 0–30 mm h^{-1} (1800:00–1830:00 UTC 11 Mar 2017) coupled with the patterns in (a), and the deep convective clouds (200–220 K) on *Meteosat-11* images from (c) 1745:00 and (d) 1800:00 UTC 11 Mar 2017 corresponding to the small squall line and convection cells in (a).

previous one increases confidence in the assumption that there is a corresponding relation between the CS severity (represented by brightness temperature value) and the associated surface strong wind speed.

c. Submesoscale wind patterns accompanied by various precipitation

Figures 4a and 5a illustrate submesoscale wind patterns detected on VV-pol Sentinel-1 images from 1800:35 UTC and 1801:00 UTC, respectively, 11 March 2017. They are observed as small squall lines (about 50 km) and convection cells (from several kilometers to about 50 km). The wind intensity of the patterns varies from 10 to 25 m s^{-1}. Because of the high spatial resolution, one can note the spots with high wind intensity (20–25 m s^{-1}). Light rainfall is observed in Fig. 4b for the small squall line and some convection cells (Fig. 4a), while the corresponding moderate and heavy precipitation (5–25 mm h^{-1}) are noted for the other cells. The associated precipitation with the patterns in Fig. 5a

varies from moderate to high intensity (5–50 mm h^{-1}), as shown in Fig. 5b.

Deep convective clouds corresponding to the small squall lines and convection cells are detected on *Meteosat-11* images from 1745:00 and 1800:00 UTC (Figs. 4c,d and 5c,d). The change of convective clouds during 15 min is particularly noted for the coldest spots (about 200 K). Like the previous cases, the location of the coldest convective spots and that of the high wind intensity patterns are very close. This is particularly evident when the time gap between Sentinel-1 and *Meteosat-11* is small, for example, Sentinel-1 1800:35 UTC (Fig. 4a) versus Meteosat 1800:00 UTC (Fig. 4d), and Sentinel-1 1801:00 UTC (Fig. 5a) versus Meteosat 1800:00 UTC (Fig. 5d).

Submesoscale wind patterns detected on the HH-pol Sentinel-1 image (IWS; GRD-HR) from 0530:43 UTC 12 December 2016 are shown in Figs. 6a and 6b. Various GPM precipitation (Fig. 6c) varying from light to heavy intensity (0–25 mm h^{-1}) are associated with the patterns.
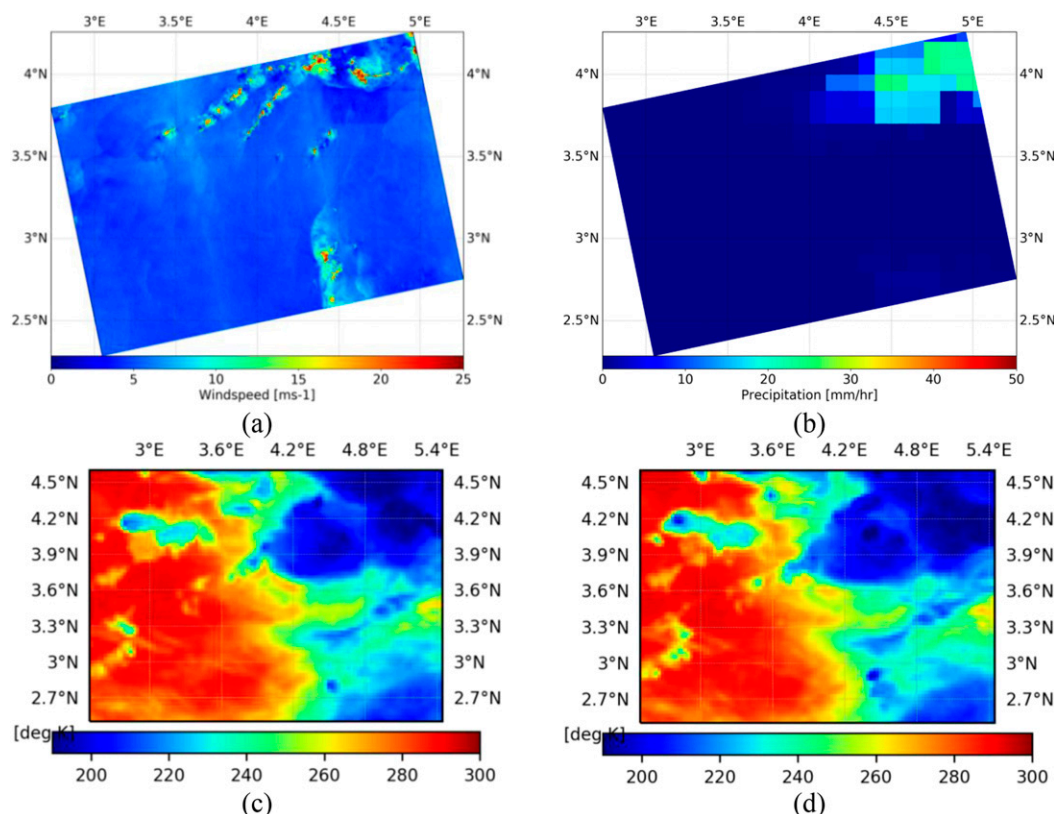
FIG. 5. (a) Detection of submesoscale wind patterns observed as small squall lines and convection cells on a (VV-pol) Sentinel-1 image (IWS; GRD-HR) from 1801:00 UTC 11 Mar 2017, (b) various GPM–IMERG precipitation of 0–50 mm h^{-1} (1800:00–1830:00 UTC 11 Mar 2017) coupled with the patterns in (a), and the deep convective clouds (200–220 K) on *Meteosat-11* images from (c) 1745:00 and (d) 1800:00 UTC 11 Mar 2017 corresponding to the small squall line and convection cells in (a).

Some convection cells have the shape of a bow echo as in Fig. 3a, but their size is smaller (about 50 km). The wind speeds estimated by the Sapp model in Fig. 6a (with the GFS wind direction input) and Komarov model in Fig. 6b (without wind direction input) are very close. This illustrates that the large-scale GFS wind direction should not be a major issue for wind speed estimation, as also indicated in La et al. (2018).

Figures 6d and 6e illustrate deep convective clouds corresponding to the convection cells in Fig. 6a. Spots with the lowest temperature (about 200 K) have an agreement not only in spatial location but also in size (several kilometers) with the strong wind ones (20–25 m s^{-1}) in Fig. 6a. This is particularly noted in the zones about 2.8°N, 2.3°E and about 2°N, 3°E.

4. Discussion

Because of the high spatial resolution of Sentinel-1, the small-scale (pattern) spots with high wind intensity (20–25 m s^{-1}) were detected on Sentinel-1 images, which has not been reported for the ASCAT (Kilpatrick and Xie 2015). The additional use of Meteosat images leads to the assumption of the relationship between the wind patterns on the sea surface and deep convective clouds (aloft). This (space) correlation was discussed in (Kilpatrick and Xie 2015); however, only the relationship between moderate surface winds (about 10–15 m s^{-1}) and mesoscale convective downdrafts was reported.

The assumption presented in this study that wind patterns on Sentinel-1 images are produced by the CS downdrafts hitting the sea surface is strengthened by the agreement in spatial location and sometimes in shape between wind patterns and deep convective clouds in Meteosat images. In particular, the spots with high wind intensity (20–25 m s^{-1}) and those with the lowest brightness temperature (coldest spots with about 200 K) on Meteosat images have very close spatial locations. The lower wind intensity zones (10–15 m s^{-1}), meanwhile, correspond to the convective clouds with higher brightness temperatures (more than 210 K). This illustrates that
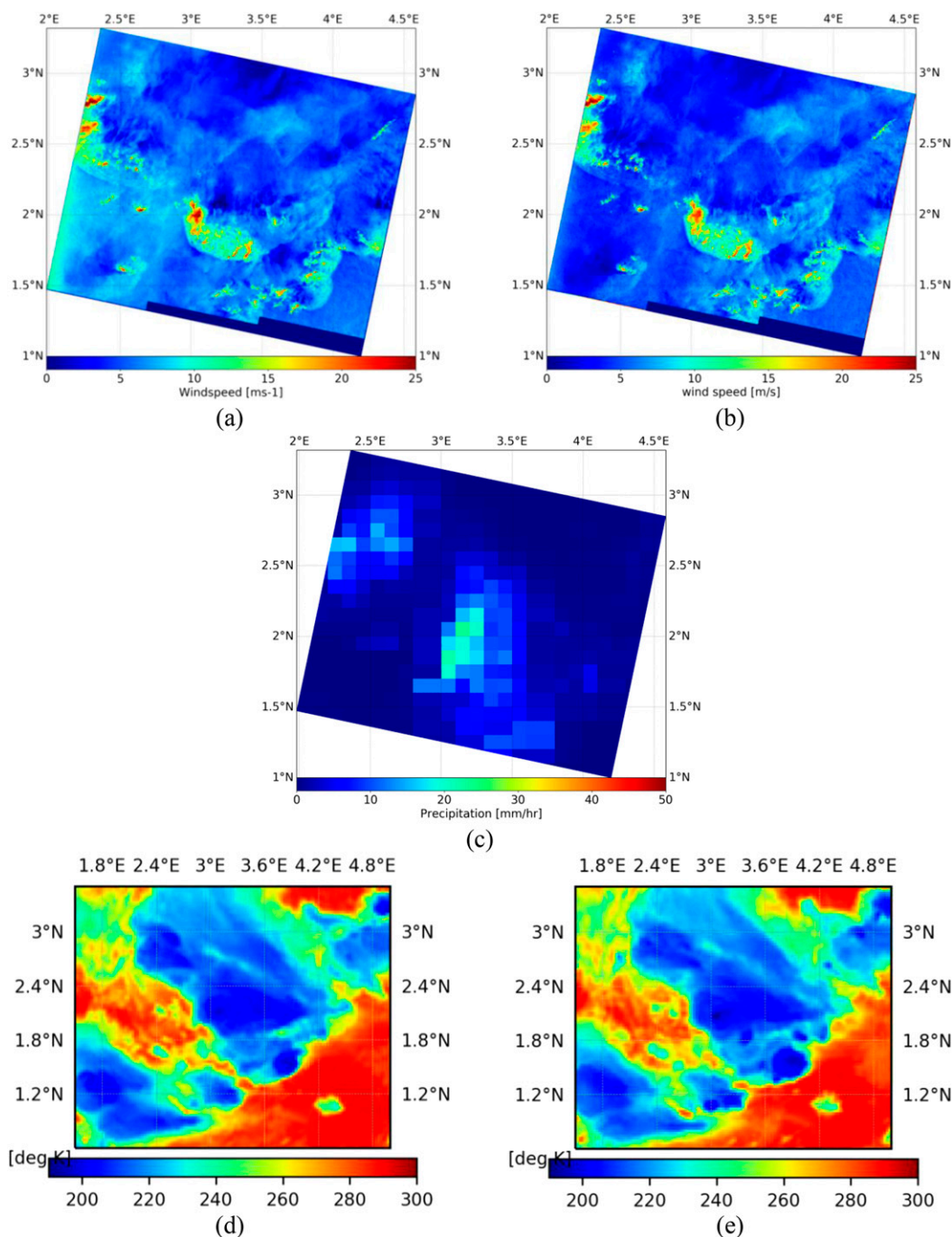
FIG. 6. Detection of submesoscale wind patterns observed as small bow echoes and convection cells on an (HH-pol) Sentinel-1 image (IWS; GRD-HR) from 0530:43 UTC 12 Dec 2016: wind speed estimated (a) by the Sapp model with the GFS wind direction input and (b) by the Komarov model without wind direction input, (c) various GPM–IMERG precipitation of 0–25 mm h^{-1} (0530:00–0600:00 UTC 12 Dec 2016) coupled with the patterns in (a), and deep convective clouds (200–220 K) on *Meteosat-11* images from (d) 0515:00 and (e) 0530:00 UTC 12 Dec 2016 corresponding to the small bow echoes and convection cells in (a).

there may be a correlation between the CS severity (represented by the lowest temperature spots) and surface wind pattern intensity. The deeper (or higher) the convective clouds are, the stronger the associated surface wind speed is.

During 15 min (Meteosat sampling frequency), the evolution of convective clouds mainly occurs at the coldest spots (about 200-K brightness temperature). The latter corresponds to the spots with high wind intensity (20–25 m s^{-1}). This is more evident when the time gap between Sentinel-1 and Meteosat is small. Also, it raises the question about the monitoring of the convective cloud evolution and the change of the CS-associated surface wind patterns observed by two successive SAR images. The first results regarding this topic were published in La and Messager (2020). They investigated the evolution of surface wind patterns by comparisons between Sentinel-1 and *RadarSat-2* images with two cases of observation time differences (about 1 and 5 min). They illustrated that the evolution of wind patterns (both high- and moderate-wind spots) was noted in both cases; however, it is more significant for a long-time delay. In particular, the change of high-wind spots (15–25 m s^{-1}) occurs more quickly than the moderate-wind spots (10–15 m s^{-1}), especially in the case of the 1-min difference. As discussed in La and Messager (2020), the small-scale (convective scale) downdrafts with high intensity (associated with the coldest convective clouds) reach the sea surface more quickly than the mesoscale ones, and thereby the high-wind spots induced by the former will be weakened more rapidly than those due to the latter. This observation matches the time series measurements of wind speed of a moored buoy in the tropics (Portabella et al. 2012).

The corresponding precipitation (GPM–IMERG) to surface wind patterns is diverse (Figs. 2b–5b and 6c), including light, moderate, and intense precipitation. As well as the relation between deep convective clouds and surface wind patterns, the one between the latter and precipitation is complex. Precipitation is supposed to strengthen the air cooling that falls and hits the sea surface. This process may produce surface strong winds or gusts. Thus, there are three scenarios to explain the diversity of precipitation intensities: (i) wind gust may occur without precipitation due to the evaporation of the latter before it hits the surface, (ii) precipitation may reach the surface without strong winds due to air stratification effects, and (iii) both strong winds and precipitation occur at the sea surface. Indeed, these scenarios match the time series measurements of wind speed and rain rate of a moored buoy (Portabella et al. 2012). The high wind speed may be accompanied by light, moderate, and intense precipitation, and heavy rain occurs

without strong winds. To understand more deeply the relationship between strong surface winds (associated with the CS) and precipitation, statistical analysis between Sentinel-1-based wind speed and rain rate obtained from the GPM–IMERG and/or the Next-Generation Weather Radar (NEXRAD) should be carried out. Such a study should take into account two important issues of observation time gaps and differences in spatial resolution between Sentinel-1 and GPM–IMERG (or NEXRAD). Additionally, it should envisage the dependence of IMERG data on the Meteosat data since the former uses the infrared radiances (obtained by Meteosat) as part of its retrieval system to fill in gaps between GPM observations (Huffman et al. 2015).

5. Conclusions and perspectives

The current paper proposed the use of Sentinel-1 (SAR) images for the detection of wind patterns (or cold pools) produced by the CS downdrafts hitting the sea surface. Thanks to the high spatial resolution and a large swath of Sentinel-1, various types of wind patterns in terms of size and shape were observed: a mesoscale (>100 km) squall line, a mesoscale bow echo, and many submesoscale (<100 km) convection cells. The wind intensity of the patterns varies from 10 to 25 m s^{-1}. In particular, the spots with high winds (20–25 m s^{-1}) can be detected on high-resolution Sentinel-1 images, which has not been reported in the literature. The assumption that surface wind patterns on Sentinel-1 images are associated with the CS was strengthened by the agreement in spatial location (and sometimes in shape) between the patterns and deep convective clouds detected on Meteosat infrared images. This is particularly noted for the pattern spots with high winds and the convective ones with the lowest brightness temperature (about 200 K). Additionally, between two Meteosat images (15- min difference in observation time), the evolution was significantly noted for the coldest convective spots.

There are some important aspects of this topic that should be clarified in future studies, including the relationship between deep convective clouds and the associated surface wind patterns in terms of shape, size, and wind intensity. For instance, under what conditions the deep convective clouds observed on Meteosat images in the forms of a squall line, a bow echo, or submesoscale convection cells produce wind patterns (cold pools) on the sea surface and which wind intensity can be. In addition, the study of the evolution of surface wind patterns observed by successive SAR images should be carried out with many cases. Likewise, statistical analysis of wind gust–rain rate relationship (based on SAR

and GPM/NEXRAD, respectively) should be performed to understand the correlation between them. Last, the method proposed in this paper may be significantly useful to improve mesoscale forecast, in particular for the CS-associated variability, which is currently very badly represented in the models. Indeed, the data assimilation of the combined view of sea surface wind (observed by SAR) and the associated brightness temperature at cloud top height could introduce a high level of relevance for the NWP regional forecast at mesoscale and submesoscale. The proposed method lets an identification of the CS having impact and dynamics down to the sea surface and permits to introduce a kind of three-dimensional information about the CS activity as well as their location, evolution, and displacement, which is highly valuable for 4D-Var assimilation method.

REFERENCES

Alpers, W., W. K. Wong, K.-F. Dagestad, and P. W. Chan, 2015: Study of a wind front over the northern South China Sea generated by the freshening of the north-east monsoon. *Bound.-Layer Meteor.*, **157**, 125–140, https://doi.org/10.1007/s10546-015-0050-8.

——, B. Zhang, A. Mouche, K. Zeng, and P. W. Chan, 2016: Rain footprints on C-band synthetic aperture radar images of the ocean—Revisited. *Remote Sens. Environ.*, **187**, 169–185, https://doi.org/10.1016/j.rse.2016.10.015.

Collecte Localisation Satellites, 2016: Sentinel-1 product definition. ESA Doc. S1-RS-MDA-52-7440, 120 pp., https://sentinel.esa.int/documents/247904/1877131/Sentinel-1-Product-Definition.

Contreras, R. F., and W. J. Plant, 2006: Surface effect of rain on microwave backscatter from the ocean: Measurements and modeling. *J. Geophys. Res.*, **111**, C08019, https://doi.org/10.1029/2005JC003356.

Cotton, W. R., G. Bryan, and S. C. van den Heever, 2011: Mesoscale convective systems. *Storm and Cloud Dynamics—The Dynamics of Clouds and Precipitating Mesoscale Systems*, International Geophysics Series, Vol. 99, Academic Press, 455–526.

Du, Y., P. W. Vachon, and J. Wolfe, 2002: Wind direction estimation from SAR images of the ocean using wavelet analysis. *Can. J. Remote Sens.*, **28**, 498–509, https://doi.org/10.5589/m02-029.

Fetterer, F., D. Gineris, and C. C. Wackerman, 1998: Validating a scatterometer wind algorithm for ERS-1 SAR. *IEEE Trans.*

Geosci. Remote Sens., **36**, 479–492, https://doi.org/10.1109/36.662731.

Hersbach, H., 2008: CMOD5.N: A C-band geophysical model function for equivalent neutral wind. ECMWF Tech. Memo. 554, 22 pp., https://doi.org/10.21957/mzcfm6jfl.

——, A. Stoffelen, and S. De Haan, 2007: An improved C-band scatterometer ocean geophysical model function: CMOD5. *J. Geophys. Res.*, **112**, C03006, https://doi.org/10.1029/2006JC003743.

Huffman, G. J., D. T. Bolvin, E. J. Nelkin, and J. Tan, 2015: Integrated Multi-satellitE Retrievals for GPM (IMERG) technical documentation. IMERG Tech. Doc., 64 pp., https://gpm.nasa.gov/sites/default/files/document_files/IMERG_doc_190313.pdf.

Kastman, S. J., S. P. Market, I. N. Fox, A. L. Foscato, and R. A. Lupo, 2017: Lightning and rainfall characteristics in elevated vs. surface based convection in the Midwest that produce heavy rainfall. *Atmosphere*, **8**, 36, https://doi.org/10.3390/atmos8020036.

Kilpatrick, T. J., and S.-P. Xie, 2015: ASCAT observations of downdrafts from mesoscale convective systems. *Geophys. Res. Lett.*, **42**, 1951–1958, https://doi.org/10.1002/2015GL063025.

King, G. P., M. Portabella, W. Lin, and A. Stoffelen, 2017: Correlating extremes in wind and stress divergence with extremes in rain over the tropical Atlantic. EUMETSAT Ocean and Sea Ice SAF Scientific Rep. OSI_AVS_15_02, 36 pp.

Klein, C., D. Belušić, and C. M. Taylor, 2018: Wavelet scale analysis of mesoscale convective systems for detecting deep convection from infrared imagery. *J. Geophys. Res. Atmos.*, **123**, 3035–3050, https://doi.org/10.1002/2017JD027432.

Koch, W., 2004: Directional analysis of SAR images aiming at wind direction. *IEEE Trans. Geosci. Remote Sens.*, **42**, 702–710, https://doi.org/10.1109/TGRS.2003.818811.

Komarov, A. S., V. Zabeline, and D. G. Barber, 2014: Ocean surface wind speed retrieval from C-band SAR images without wind direction input. *IEEE Trans. Geosci. Remote Sens.*, **52**, 980–990, https://doi.org/10.1109/TGRS.2013.2246171.

Kuchera, E. L., and M. D. Parker, 2006: Severe convective wind environments. *Wea. Forecasting*, **21**, 595–612, https://doi.org/10.1175/WAF931.1.

La, T. V., and C. Messager, 2020: Convective system sea surface wind pattern detection and variability observation from a combination of Sentinel-1 and Radarsat-2 images. *Remote Sens. Lett.*, **11**, 446–454, https://doi.org/10.1080/2150704X.2020.1731621.

——, A. Khenchaf, F. Comblet, and C. Nahum, 2017: Exploitation of C-band Sentinel-1 images for high-resolution wind field retrieval in coastal zones (Iroise Coast, France). *IEEE J. Sel. Top. Appl. Earth Obs. Remote Sens.*, **10**, 5458–5471, https://doi.org/10.1109/JSTARS.2017.2746349.

——, C. Messager, M. Honnorat, and C. Channelliere, 2018: Detection of convective systems through surface wind gust estimation based on Sentinel-1 images: A new approach. *Atmos. Sci. Lett.*, **19**, e863, https://doi.org/10.1002/asl.863.

Li, X., X. Yang, W. Zheng, J. A. Zhang, L. J. Pietrafesa, and W. G. Pichel, 2015: Synergistic use of satellite observations and numerical weather model to study atmospheric occluded fronts. *IEEE Trans.Geosci. Remote Sens.*, **53**, 5269–5279, https://doi.org/10.1109/TGRS.2015.2420312.

——, W. Zheng, X. Yang, and L. J. Pietrafesa, 2017: Sea fetch observed by synthetic aperture radar. *IEEE Trans Geosci. Remote Sens.*, **55**, 272–279, https://doi.org/10.1109/TGRS.2016.2605670.

Liu, C., E. J. Zipser, and S. W. Nesbitt, 2007: Global distribution of tropical deep convection: Different perspectives from TRMM

infrared and radar data. *J. Climate*, **20**, 489–503, https://doi.org/10.1175/JCLI4023.1.

Met Office, 2007: Water. Fact sheet 3—Water in the atmosphere, National Meteorological Library and Archive, 26 pp., https://www.metoffice.gov.uk/binaries/content/assets/metofficegovuk/pdf/research/library-and-archive/library/publications/factsheets/factsheet_3-water-in-the-atmosphere.pdf.

Mohr, S., M. Kunz, A. Richter, and B. Ruck, 2017: Statistical characteristics of convective wind gusts in Germany. *Nat. Hazards Earth Syst. Sci.*, **17**, 957–969, https://doi.org/10.5194/nhess-17-957-2017.

Montuori, A., P. De Ruggiero, M. Migliaccio, S. Pierini, and G. Spezie, 2013: X-band COSMO-SkyMed wind field retrieval, with application to coastal circulation modeling. *Ocean Sci.*, **9**, 121–132, https://doi.org/10.5194/os-9-121-2013.

Mouche, A. A., F. Collard, B. Chapron, K.-F. Dagestad, G. Guitton, J. A. Johannessen, and V. Kerbaol, 2012: On the use of Doppler shift for sea surface wind retrieval from SAR. *IEEE Trans. Geosci. Remote Sens.*, **50**, 2901–2909, https://doi.org/10.1109/TGRS.2011.2174998.

——, B. Chapron, B. Zhang, and R. Husson, 2017: Combined co- and cross-polarized SAR measurements under extreme wind conditions. *IEEE Trans. Geosci. Remote Sens.*, **55**, 6746–6755, https://doi.org/10.1109/TGRS.2017.2732508.

Portabella, M., A. Stoffelen, A. Verhoef, and W. Lin, 2012: Rain effects on ASCAT retrieved winds: Towards an improved quality control. *IEEE Trans. Geosci. Remote Sens.*, **50**, 2495–2506, https://doi.org/10.1109/TGRS.2012.2185933.

Priftis, G., T. J. Lang, and T. Chronis, 2018: Combining ASCAT and NEXRAD retrieval analysis to explore wind features of mesoscale oceanic systems. *J. Geophys. Res. Atmos.*, **123**, 10 341–10 360, https://doi.org/10.1029/2017JD028137.

Quilfen, Y., B. Chapron, T. Elfouhaily, K. Katsaros, and J. Tournadre, 1998: Observation of tropical cyclones by high-resolution scatterometry. *J. Geophys. Res.*, **103**, 7767–7786, https://doi.org/10.1029/97JC01911.

Raj, J., H. K. Bangalath, and G. Stenchikov, 2019: West African monsoon: Current state and future projections in a high-resolution AGCM. *Climate Dyn.*, **52**, 6441–6461, https://doi.org/10.1007/s00382-018-4522-7.

Sapp, J. W., S. O. Alsweiss, Z. Jelenak, P. S. Chang, S. J. Frasier, and J. Carswell, 2016: Airborne co-polarization and cross-polarization observations of the ocean-surface NRCS at C-band. *IEEE Trans. Geosci. Remote Sens.*, **54**, 5975–5992, https://doi.org/10.1109/TGRS.2016.2578048.

Stoffelen, A., and D. Anderson, 1997: Scatterometer data interpretation: Estimation and validation of the transfer function CMOD4. *J. Geophys. Res.*, **102**, 5767–5780, https://doi.org/10.1029/96JC02860.

Sultan, B., and S. Janicot, 2003: The West African monsoon dynamics. Part II: The "preonset" and "onset" of the summer monsoon. *J. Climate*, **16**, 3407–3427, https://doi.org/10.1175/1520-0442(2003)016<3407:TWAMDP>2.0.CO;2.

Weisman, M. L., and R. J. Trapp, 2003: Low-level mesovortices within squall lines and bow echoes. Part I: Overview and dependence on environmental shear. *Mon. Wea. Rev.*, **131**, 2779–2803, https://doi.org/10.1175/1520-0493(2003)131<2779:LMWSLA>2.0.CO;2.

Xu, F., X. Li, P. Wang, J. Yang, W. G. Pichel, and Y. Q. Jin, 2015: A backscattering model of rainfall over rough sea surface for synthetic aperture radar. *IEEE Trans. Geosci. Remote Sens.*, **53**, 3042–3054, https://doi.org/10.1109/TGRS.2014.2367654.